

Anatomy X-Net: A Semi-Supervised Anatomy Aware Convolutional Neural Network for Thoracic Disease Classification

Uday Kamal, Mohammad Zunaed, Nusrat Binta Nizam, and Taufiq Hasan, *Senior Member, IEEE*

Abstract—Thoracic disease detection from chest radiographs using deep learning methods has been an active area of research in the last decade. Most previous methods attempt to focus on the diseased organs of the image by identifying spatial regions responsible for significant contributions to the model’s prediction. In contrast, expert radiologists first locate the prominent anatomical structures before determining if those regions are anomalous. Therefore, integrating anatomical knowledge within deep learning models could bring substantial improvement in automatic disease classification. This work proposes an anatomy-aware attention-based architecture named Anatomy X-Net, that prioritizes the spatial features guided by the pre-identified anatomy regions. We leverage a semi-supervised learning method using the JSRT dataset containing organ-level annotation to obtain the anatomical segmentation masks (for lungs and heart) for the NIH and CheXpert datasets. The proposed Anatomy X-Net uses the pre-trained DenseNet-121 as the backbone network with two corresponding structured modules, the Anatomy Aware Attention (AAA) and Probabilistic Weighted Average Pooling (PWAP), in a cohesive framework for anatomical attention learning. Our proposed method sets new state-of-the-art performance on the official NIH test set with an AUC score of 0.8439, proving the efficacy of utilizing the anatomy segmentation knowledge to improve the thoracic disease classification. Furthermore, the Anatomy X-Net yields an averaged AUC of 0.9020 on the Stanford CheXpert dataset, improving on existing methods that demonstrate the generalizability of the proposed framework.

Index Terms—Semi-supervised learning, anatomy-aware attention, lung and heart attention vectors.

I. INTRODUCTION

CHEST radiography (CXR) is the most commonly used primary screening tool for assessing thoracic diseases such as pneumonia, pneumothorax, pulmonary edema, consolidation, infiltration, emphysema, and pleural effusions [1]. Each year a massive number of CXRs are produced, and the diagnosis is performed mainly by radiologists. Diagnosis of CXRs requires a high degree of skills and concentration. With the severe shortage of expert radiologists, especially in developing countries, computer-aided disease detection from chest radiographs is considered the future of medical diagnosis [2], [3]. Advancement in deep learning and artificial intelligence offers several ways of rapid, accurate, and reliable screening techniques [4]. These techniques can significantly impact the health systems in the resource-constrained regions of the world

Uday kamal, Mohammad Zunaed, Nusrat Binta Nizam, and Taufiq Hasan are with the Department of Biomedical Engineering, Bangladesh University of Engineering and Technology, Dhaka-1205, Bangladesh. (e-mails: udday2014@gmail.com, rafizunaed@gmail.com, nusratbintanizam023@gmail.com, taufiq@bme.buet.ac.bd.)

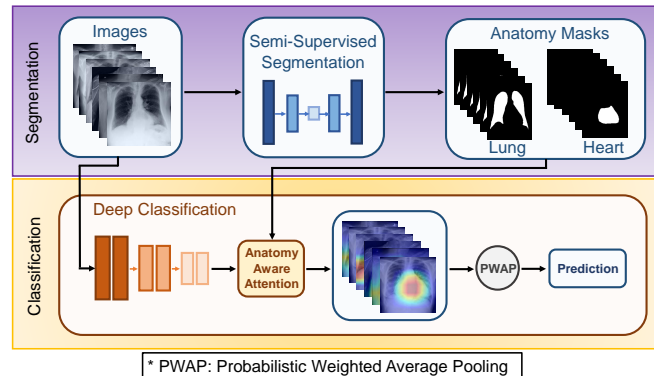


Fig. 1: Overview of the proposed semi-supervised anatomy-aware attention-based thoracic disease classification framework. A semi-supervised technique is utilized to generate anatomy masks for unannotated CXR images. Then, with the help of our proposed novel anatomy-aware attention module, anatomical information is integrated into the classification network for pathology detection.

where there is a high prevalence of thoracic diseases and a shortage of expert radiologists.

Driven by many publicly accessible large-scale CXR datasets, a significant amount of research efforts have been carried out for the automatic diagnosis of thoracic diseases. Wang et al. [5] first announced the ChestX-ray14 dataset and proposed a unified weakly-supervised classification network by introducing various multi-label DCNN losses based on ImageNet [6] pre-trained deep CNN models [7], [8], [9]. Tang et al. [10] used an attention-guided curriculum learning method to identify the disease category and localize the lesion areas. LLAGnet [11] is a novel lesion location attention guided network containing two corresponding attention modules which focus on the discriminative features from lesion areas for multi-label thoracic disease classification in CXRs. Guan et al. [12] proposed a category-wise residual attention learning (CRAL) framework for multi-label thoracic disease classification, which can suppress the obstacles of irrelevant classes by endowing small weights to the corresponding feature maps. In [13], Wang et al. proposed a DenseNet-121 based triple learning approach that integrates three attention modules which are unified for channel-wise, element-wise, and scale-wise attention learning.

In medical practice, interpretation of chest X-rays, or any

other medical imaging modalities for that matter, requires an understanding of the relevant human anatomy that is being imaged. For example, fundamental analysis of chest X-rays involves the radiologist determining if the trachea is central, the lungs are uniformly expanded, the lung fields are clear, and the heart size is normal [14]. These and other similar observations form the basis of CXR interpretation by human vision, where it is clear that knowledge of anatomical structures is vital. However, most previous research works in automated analysis of CXRs do not consider this aspect and address the problem as any other computer vision problem. Most previous methods employed a global learning strategy [5], [15], or relied on attention mechanisms [10], [11], [16], that try to determine the spatial regions that are more responsible for model prediction. For thoracic disease classification, a lesion region is often associated with important anatomical regions, and therefore, incorporating anatomy-related information within deep learning models can potentially improve classification performance.

This paper proposes an anatomy-aware attention-based architecture named Anatomy X-Net that utilizes the anatomy segmentation information along with CXRs to classify thoracic diseases. We adopt Densenet-121 as the backbone network and incorporate two structured modules called Anatomy Aware Attention (AAA) and Probabilistic Weighted Average Pooling (PWAP) in a united framework for anatomy information learning. The AAA module reinforces the sensitivity of the different stages of the model to prioritize the anatomical location responsible for a thoracic disease. A significant challenge to integrate anatomy information into the framework is the lack of proper contour-level anatomy region annotations for large-scale datasets such as NIH [5], and CheXpert [17]. To solve this problem, we leverage a semi-supervised learning technique [18] that uses the Japanese Society of Radiological Technology (JSRT) [19] dataset to generate the anatomy segmentation masks for the NIH and CheXpert datasets. An overview of our proposed framework is presented in Fig. 1. The contributions of this paper are summarized as follows:

- We propose novel hierarchical feature-fusion-based AAA modules that calibrate the feature maps in different stages of the model based on anatomy segmentation knowledge to improve the classification performance.
- We incorporate novel PWAP pooling modules that tweak the relevant areas of the feature space before pooling.
- Our Anatomy X-Net achieves new state-of-the-art performance with an AUC score of 0.8439 on the official NIH test set, demonstrating the efficacy of utilizing the anatomy segmentation knowledge to improve the thoracic disease classification. Our Anatomy X-Net reaches the average AUC score of 0.9020 on the official validation split of the Stanford CheXpert dataset, which demonstrates the generalizability of our proposed framework.

II. RELATED WORK

A. Organ Segmentation from Chest Radiographs

There are several methods for organ segmentation from a CXR image. A hybrid approach by Shao et al. [20], combining active shape and appearance models, achieved a Jaccard score

of 0:946 on the Segmentation in Chest Radiographs (SCR) dataset [21]. Ibragimov et al. [22] combined landmark-based segmentation and a random forest classifier to achieve an overlap score of 0:953. Xu et al. [23] proposed an active shape framework addressing the initialization dependency of these models that achieved an overlay score of 0:954. In the advent of deep learning, Convolutional neural network (CNN) based segmentation of medical images has attracted wider attention of researchers. An end-to-end contour-aware CNN-based segmentation method is shown to provide organ contour information and improve the segmentation accuracy [24]. In [25], lung segmentation is performed from CXRs using Generative adversarial networks (GAN). However, this model is not generalizable to new datasets. Two-stage deep learning techniques such as patch classification and reconstruction of lung fields can be used for lung segmentation from CXR images [26]. The U-net architecture is used for the detection and segmentation of pneumothorax on CXRs [27]. In [28], an adaptive preprocessing with CNN is used for the segmentation of lung on contrast-enhanced binarized images.

B. Disease Classification from Chest Radiographs

Many signal processing and deep learning approaches have been proposed to classify thoracic diseases in recent years. Wang et al. [5] utilized the ImageNet [6], pre-trained deep CNN models, i.e., AlexNet, VGGNet [7], GoogLeNet [8], ResNet [9], to perform multi-label thoracic disease classification. Yao et al. [29] proposed a joint variant of DenseNet [30] and Long-Short Term Memory Network (LSTM) [31] to focus on the label correlation among image labels. Wang et al. [32] proposed the TieNet (Text Image Embedding Network), an end-to-end CNN-RNN framework, for learning to embed visual images and text reports for image classification and report generation. Tang et al. [10] identify the disease category and localize the lesion areas through an attention-guided curriculum learning method.

In [33], multiple feature integration is presented using shallow handcrafted techniques and a pre-trained deep CNN model. The classification approach integrates four types of local and deep features extracted from SIFT, GIST, LBP, and HOG, and convolutional CNN features. This method misses different shallow feature descriptors and in-depth features, which may include important information for classification. Segmentation-based deep fusion network (SDFN) [34] is a method that leverages the domain knowledge and the higher-resolution information of local lung regions. Using Lung Region Generator (LRG), the local lung regions are identified, and discriminative features are extracted using two CNN models. DualCheXNet [35] is an approach that enables two different feature fusion operations, such as feature-level fusion (FLF) and decision level fusion (DLF), which form the complementary feature learning embedded in the network. This complementary feature learning with two asymmetric deep CNNs is beneficial to multi-label medical image classification, but more sophisticated approaches like the anatomical approach remain unexplored. LLAGnet [11] is a novel lesion location attention guided network containing two corresponding attention modules which focus on the discriminative

features from lesion locations for multi-label thoracic disease classification in CXRs. However, in this method, the classification accuracy of “Infiltration” and “Consolidation” is not satisfactory because of various types of textures.

Guan et al. [12] proposed a category-wise residual attention learning (CRAL) framework for multi-label thoracic disease classification. CRAL alleviates irrelevant classes by assigning small weights to the corresponding feature representations. Rajpurkar et al. [15] exploited a modified 121-layer DenseNet named CheXNet, for diagnosis of all 14 pathologies in the ChestXray14 dataset, especially for “Pneumonia”. However, As mentioned in [15], the significance of the comparison between CheXNet and human labeling was compromised by the fact that only the frontal views of radiographs were presented to the radiologists. In [13], a triple learning approach integrating a unified channel-wise, element-wise, and scale-wise attention modules are used. They can simultaneously learn disease-discriminative channels, locations, and scales for effective diagnosis. However, the element-wise attention map is chaotic, and for this reason, the hernia case can not be classified correctly. Yan et al. [16] proposed a weakly supervised deep learning framework equipped with the squeeze and excitation blocks, multi-map transfer, and max-min pooling for classifying thoracic diseases as well as localizing suspicious lesion regions. Luo et al. [36] adopted task-specific adversarial training and an uncertainty-aware temporal ensemble of model predictions to address the domain and label discrepancies across different datasets. To handle label uncertainty on the CheXpert dataset, Irvin et al. [17] trained a DenseNet-121 on CheXpert with various labeling policies such as U-Ignore, U-Ones, and U-Zeros policies. Pham et al. [37] exploits dependencies among abnormality labels and utilized label smoothing technique for better handling of uncertain samples in the CheXpert dataset.

III. METHODOLOGY

A. Motivation

Successful implementation of deep learning-based thoracic disease classification approaches requires not only higher accuracy but also interpretability. Real-world radiologists locate the vital anatomy regions first and then determine if those regions have abnormalities. None of the previous works discussed in Section II-B integrates anatomy knowledge into their framework. In this work, we aim to bridge this gap between human experts and the ML models by incorporating prior information of the anatomical regions into the network. However, the existing annotated anatomy segmentation datasets are very small in size. Using them in a supervised learning environment will limit the model’s generalizability. Thus, we leverage a semi-supervised learning technique [18] that can work on a minimal amount of annotated datasets (e.g., JSRT). However, the imperfect mask segmentation from the semi-supervised-based approach can pose a challenge to the classification network if they are passed as it is. Also, we can not perform segmentation of the vital anatomy regions (e.g., lung, heart) and provide only those regions as input to the network. This will constrain the field of view for the

network and may lead to difficulty in learning to identify and differentiate the anatomy regions. Therefore, we propose an anatomy-aware attention-based architecture named Anatomy X-Net that integrates anatomy segmentation knowledge into different stages of the network to prioritize the spatial regions generally responsible for the pathologies.

B. Semi-supervised Anatomy Segmentation Network

For semi-supervised segmentation of anatomy regions, we adopted the method from [18]. The architecture for semi-supervised segmentation is illustrated in Fig. 2. The segmentation setting contains two distinct subsets: L , containing annotated CXR images ω_L and their corresponding ground-truth masks θ_L , and u , which contains unannotated CXR images ω_u . The first generator (G_{CM}) learns a mapping from a CXR image to its anatomy segmentation masks, while the second generator (G_{MC}) learns to map a segmentation mask to its CXR image. The first discriminator (D_M) tries to differentiate these generated masks from the real segmentation masks. Similarly, the second discriminator (D_C) receives a CXR image as input and predicts whether this image is real or generated. Cycle consistency loss enforces that feeding the segmentation masks generated by G_{CM} for a CXR image into G_{MC} returns the same CXR image. Similarly, passing back the CXR image generated by G_{MC} to G_{CM} for a segmentation mask returns the same mask.

C. Anatomy X-Net

The proposed anatomy-aware thoracic disease classification network is illustrated in Figure 3. We utilized transfer learning on DenseNet-121 [30] architecture pre-trained on the ImageNet [6] and used it as our backbone model. The backbone model compresses the raw pixel-level information present in a CXR image to a high-level feature of lower-dimensional space. DenseNet-121 consists of four dense blocks (DB). The proposed AAA attention module operates on the high-level feature space encoded by these DBs. AAA enforces attention supervision to the salient regions of the feature space guided by the anatomy segmentation masks. Due to hardware constraints, we performed downsampling and upsampling on the anatomy segmentation masks and feature space to an intermediate shape before passing them to an AAA module. These recalibrated feature spaces from each of the AAA modules are pooled by PWAP layers and concatenated together. Finally, this concatenated feature vector is passed to a dense layer for pathology classification. The different components of the proposed Anatomy X-Net architecture is described in the following sub-sections.

Anatomy Aware Attention (AAA) Module:

The AAA module consists of Probabilistic Weighted Average Pooling (PWAP) modules, attention vector encoders, and batch normalization layers [38]. It takes the upsampled high-level feature maps ($H \times W \times C$) generated by the backbone model and the downsampled anatomy segmentation masks ($H \times W \times 2$) as inputs. Using a PWAP module, the feature map is pooled to a $1 \times 1 \times C$ dimension feature vector V . This feature vector V is then passed through three different attention vector

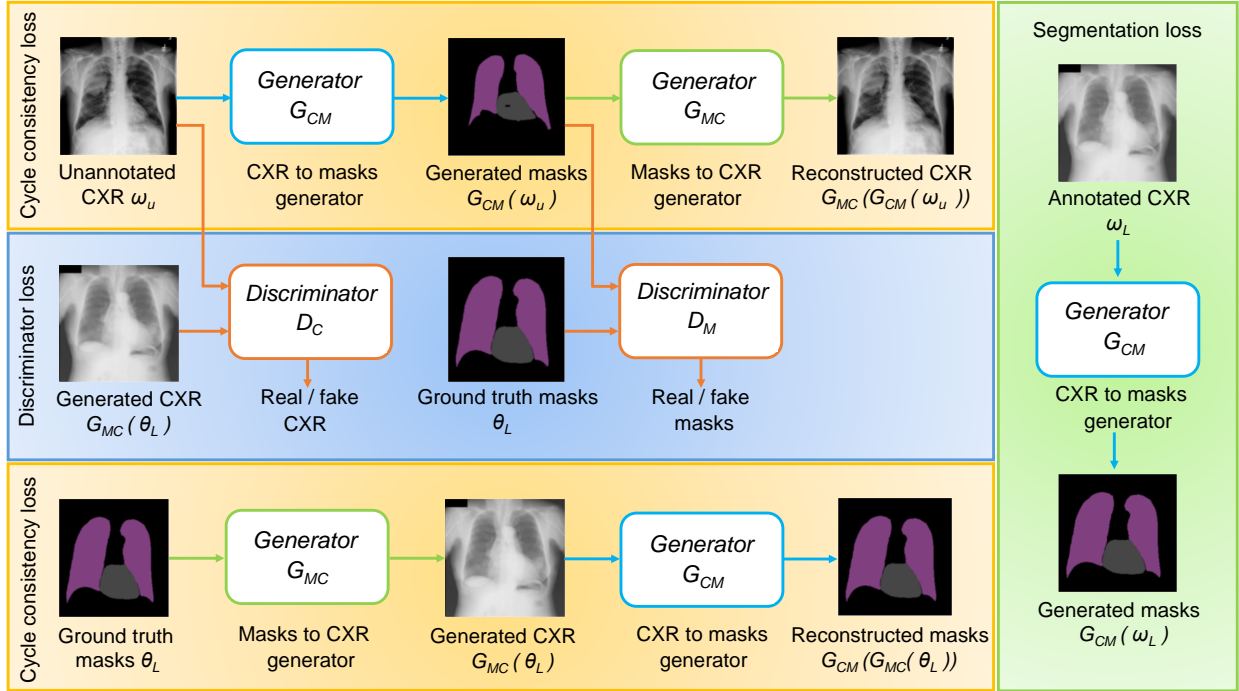


Fig. 2: Overview of the semi-supervised anatomy segmentation architecture. The pipeline contains four networks that are trained simultaneously.

encoders to get the attention vectors A . The attention vector encoders are inspired by the ‘‘Squeeze-and-Excitation’’ (SE) block [39].

To introduce bottleneck, feature vector V is first squeezed into dimension $1 \times 1 \times (C/r)$ and later excited back to $1 \times 1 \times C$. Here, r is the reduction ratio. Two AAA modules are used in the Anatomy X-Net. The first AAA module is used on the feature map encoded by DB-3. For this module, the value of C is 512, and r is 0.5. The second AAA module is used on the feature space derived from the DB-4. For this module, C is 1024, and r is 0.5. The detailed architecture of an attention vector encoder module is described in the Table I. From these three attention vector encoders, we get three feature vectors A , each having a dimension of $1 \times 1 \times C$. Next, softmax is applied on these three attention vectors by,

$$\sigma(A_k)_i = \frac{\exp(A_k)_i}{\sum_{j=1}^3 \exp(A_j)_i}, i \in \{1, \dots, C\}, k \in \{1, 2, 3\} \quad (1)$$

Here, σ represents softmax activation function, j and k represent feature vector indices, and i represents the i^{th} channel value of a feature vector. Thus, we obtain three attention

TABLE I: ATTENTION VECTOR ENCODER STRUCTURE.

Layer (Type)	Input Shape	Output Shape
Dense-1 (Dense)	(C)	(C/r)
ReLU-1 (ReLU)	(C/r)	(C/r)
BN-1 (BN)	(C/r)	(C/r)
Dense-2 (Dense)	(C/r)	(C)
ReLU-2 (ReLU)	(C)	(C)
BN-2 (BN)	(C)	(C)

* C: Channel Dimension r: Reduction ratio

vectors where each feature value across the channel dimension depends on each other. We name these three attention vectors as lung enhancer, heart enhancer, and background suppressor denoted by A_{LE} , A_{HE} , and, A_{BKS} , respectively. These quantities are related by

$$(A_{LE})_i + (A_{HE})_i + (A_{BKS})_i = 1 \quad (2)$$

where, $i \in \{1, \dots, C\}$. Next, we denote the lung mask as M_{lung} , heart mask as M_{heart} , and any high-level feature map as F . The shape of the feature map F is $H \times W \times C$ while the shape of the masks, M_{lung} , and M_{heart} is $H \times W \times 1$. For consistent channel dimensions M_{lung} , and M_{heart} are broadcasted to the shape $H \times W \times C$. Afterwards, M_{lung} , M_{heart} , and F are element-wise multiplied with the attention vectors A_{LE} , A_{HE} , and, A_{BKS} , respectively. Thus, we obtain two anatomy attentive feature space R_{LE} , R_{HE} , and the background suppressed feature space, R_{BKS} as

$$R_{LE} = A_{LE} \odot M_{lung} \quad (3)$$

$$R_{HE} = A_{HE} \odot M_{heart} \quad (4)$$

$$R_{BKS} = A_{BKS} \odot F \quad (5)$$

where \odot represents the element-wise multiplication operation. For faster convergence and removal of any internal covariate shift among R_{LE} , R_{HE} , and R_{BKS} , batch normalization operation is applied individually. Next, we sum all of the three feature spaces and apply batch normalization once again to obtain the final feature space by

$$R = \text{BN} \left(\text{BN}(R_{LE}) + \text{BN}(R_{HE}) + \text{BN}(R_{BKS}) \right). \quad (6)$$

Here, $\text{BN}(\cdot)$ denotes the batch normalization operation. Since A_{LE} is multiplied by M_{lung} , A_{LE} provides attention to the

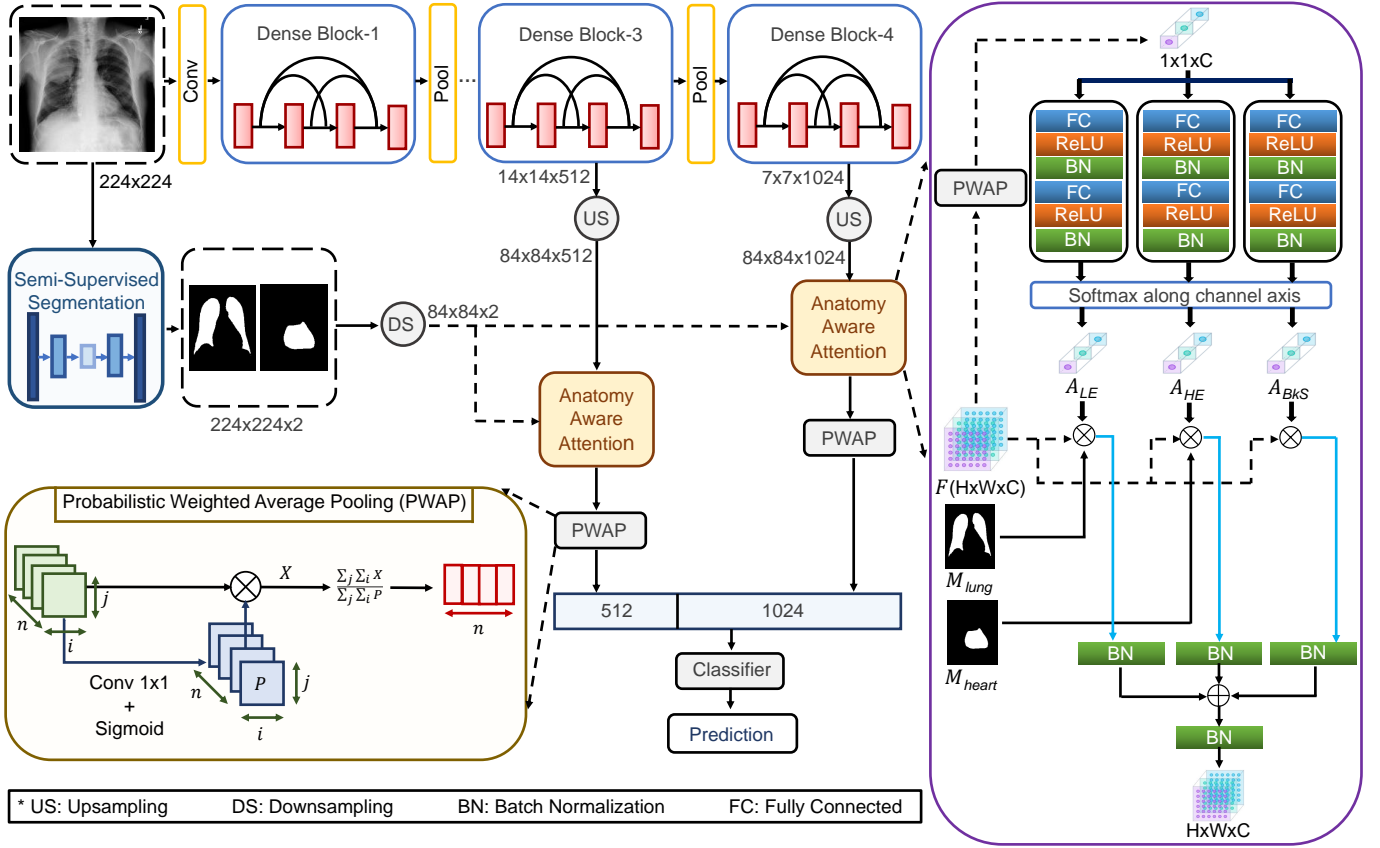


Fig. 3: The architecture of the proposed Anatomy X-Net. The inputs are the CXR images and corresponding lung and heart masks. These anatomy masks are derived from the segmentation network in a semi-supervised manner. The anatomy-aware attention modules operate on the upsampled feature spaces from DB-3 and DB-4, with the help of downsampled anatomy segmentation masks. The feature space calibrated with the supervision of anatomy knowledge from each of the anatomy-aware attention modules is pooled by the PWAP layers and concatenated. The final dense layer outputs pathology class scores by taking in these concatenated features as input. The primary objective of the framework is classification loss.

spatial regions responsible for respiratory diseases. Similarly, A_{HE} provides attention to heart-related (cardiac) diseases. For respiratory diseases, the feature values of the A_{LE} are expected to be higher compared to A_{HE} , and the opposite should be true for cardiac diseases. If a CXR contains both respiratory and cardiac pathologies, A_{LE} and A_{HE} may attain similar values. However, based on (2), increase in A_{LE} and A_{HE} will result in lower A_{BkS} . The lower attention value A_{BkS} will suppress the background areas of a CXR image.

Probabilistic Weighted Average Pooling (PWAP) Module:

The traditional global average pooling or max-pooling layer provides the same weight to all spatial regions of the input. However, in many cases, the object of interest may reside in a salient region that is more important than others. Usually, a thoracic disease is often characterized by an anatomy region and lesion areas that constitute much smaller portions than the entire image. Thus, to further enhance the attention mechanism of our Anatomy X-Net, we have used a novel PWAP module in conjunction with the AAA block. In this module, we learn the weight of each spatial position to guide Anatomy X-Net towards lesion localization during training through a 1×1 convolutional filter. The 1×1 receptive field has been

chosen as we aim to learn the weight at a single spatial position; surrounding information is unwanted. First, we get the probability map P of $H \times W \times 1$ dimension from the feature map F of dimension $H \times W \times C$ by,

$$P_{x,y,1} = \text{sigmoid} \left(\sum_{c=1}^C K_{1,1,c} * F_{x,y,c} \right), \quad x \in 1, \dots, H, \quad y \in 1, \dots, W \quad (7)$$

Here, K is the learnable convolutional filter. Afterwards, we normalize the probability map P to remove any covariance shift and obtain the weight map W of dimension $H \times W \times 1$ by

$$W_{x,y,1} = \frac{P_{x,y,1}}{\sum_{x=1}^H \sum_{y=1}^W P_{x,y,1}}. \quad (8)$$

Finally, the pooled feature map Z of size $1 \times 1 \times C$ is given by

$$Z_{1,1,c} = \sum_{x=1}^H \sum_{y=1}^W F_{x,y,c} * W_{x,y,1}. \quad (9)$$

IV. TRAINING

A. Datasets

We evaluate our proposed Anatomy X-Net on two large-scale chest X-ray datasets, NIH [5], and CheXpert [17]. The NIH dataset consists of 112,120 frontal-view CXR images from 30,805 unique patients with 14 diseases. Each CXR image in the NIH dataset is assigned with one or more pathological labels. The CheXpert dataset consists of 224,316 chest radiographs of 65,240 patients with both frontal and lateral views. We strictly follow the official split of NIH and CheXpert datasets for conducting experiments and fair comparison with previous works. The NIH dataset is split into 70% for training, 10% for validation, and 20% for testing as provided by Wang et al. [5]. U-Zeros [17] strategy is used for the CheXpert data. We report our classification model performance on the NIH test dataset and CheXpert validation dataset. We use the JSRT [19] dataset to train the segmentation model. The JSRT dataset contains 247 images in total. The segmentation annotations, including heart and lung, are obtained from [21]. We use the JSRT dataset as an annotated subset and NIH and CheXpert datasets as unannotated subsets to train the segmentation model in a semi-supervised way.

B. Training Scheme for Segmentation

For preprocessing and hyper-parameter settings, we followed the procedure described in [18]. Our data comes from three distributions: annotated CXRs (ω_L), segmentation masks of annotated CXRs (θ_L), and unannotated CXRs (ω_u). We train the generator module G_{CM} to generate segmentation masks by,

$$L_{gen}^M(G_{CM}) = \mathbb{E}_{\omega, \theta \in \omega_L, \theta_L} [\mathcal{H}(\theta, G_{CM}(\omega))] \quad (10)$$

where \mathcal{H} is the pixel-wise cross-entropy defined as,

$$\mathcal{H}(\theta, \tilde{\theta}) = - \sum_{j=1}^N \sum_{k=1}^K \theta_{j,k} \log \tilde{\theta}_{j,k} \quad (11)$$

where, $\theta_{j,k}$ and $\tilde{\theta}_{j,k}$ are the annotated segmentation masks and predicted probabilities that pixel $j \in \{1, \dots, N\}$ has label $k \in \{1, \dots, K\}$. Likewise, we employ a pixel-wise L2 norm between an annotated CXR and the CXR generated from its corresponding segmentation mask as a supervised loss to train the CXR generator G_{MC} :

$$L_{gen}^C(G_{MC}) = \mathbb{E}_{\omega, \theta \in \omega_L, \theta_L} [\|G_{MC}(\theta) - \omega\|_2^2] \quad (12)$$

Suppose that $D_M(\theta)$ is the predicted probability that segmentation masks θ correspond to an annotated CXR's segmentation mask. We define the adversarial loss for D_M as,

$$L_{disc}^M(G_{CM}, D_M) = \mathbb{E}_{\theta \in \theta_L} [(D_M(\theta) - 1)^2] + \mathbb{E}_{\omega' \in \omega_u} [(D_M(G_{CM}(\omega')))^2] \quad (13)$$

Let $D_C(\omega)$ be the predicted probability that a CXR ω is real. We get the adversarial loss for the CXR discriminator by,

$$L_{disc}^C(G_{MC}, D_C) = \mathbb{E}_{\omega' \in \omega_u} [(D_C(\omega') - 1)^2] + \mathbb{E}_{\theta \in \theta_L} [(D_C(G_{MC}(\theta)))^2] \quad (14)$$

The first cycle consistency loss measures the difference between an unannotated CXR and the regenerated CXR after passing through generators G_{CM} and G_{MC} sequentially.

$$L_{cycle}^C(G_{CM}, G_{MC}) = \mathbb{E}_{\omega' \in \omega_u} [\|G_{MC}(G_{CM}(\omega')) - \omega'\|_1] \quad (15)$$

We use cross-entropy to evaluate the difference between an annotated and regenerated segmentation mask after passing through generators G_{MC} and G_{CM} in sequence:

$$L_{cycle}^M(G_{CM}, G_{MC}) = \mathbb{E}_{\theta \in \theta_L} [\mathcal{H}(\theta, G_{CM}(G_{MC}(\theta)))] \quad (16)$$

Finally, the total loss is obtained by combining all six loss terms:

$$L_{total}(G_{CM}, G_{MC}, D_M, D_C) = L_{gen}^M(G_{CM}) + L_{gen}^C(G_{MC}) + L_{cycle}^M(G_{CM}, G_{MC}) + L_{cycle}^C(G_{CM}, G_{MC}) - L_{disc}^M(G_{CM}, D_M) - L_{disc}^C(G_{MC}, D_C) \quad (17)$$

C. Training Scheme for Classification

Multi-label Setup: The pathological labels in each CXR of the NIH dataset are expressed as a 15-dimensional label vector, $L = [l_1, \dots, l_i, \dots, l_n]$ where $l_i \in \{0, 1\}$, $n = 15$. l_i represents whether there is any pathology, i.e., 1 for presence and 0 for absence. In the case of CheXpert Dataset, L is a 13-dimensional vector. In both cases, the last element of the L vector represents the label with ‘‘No Finding’’.

Multi-label Classification Loss: The output $p(i|C)$ from the last dense layer of the Anatomy X-Net is passed through a sigmoid layer and normalized by

$$p_s(i|C) = \frac{1}{1 + \exp(-p(i|C))} \quad (18)$$

where C is a CXR image and $p_s(i|C)$ represents the probability score of C belonging to the i^{th} class, where $i \in \{1, 2, \dots, n\}$. We optimize the weight parameters of our model by minimizing the binary cross entropy (BCE) loss defined as

$$L_{cls} = -\frac{1}{n} \sum_{i=1}^n \left[l_i \log(p_s(i|C)) + (1 - l_i) \log(1 - p_s(i|C)) \right], \quad (19)$$

where l_i is the ground-truth label of the i^{th} class and n is the number of pathologies. ‘‘Cardiomegaly’’ in the NIH dataset and ‘‘cardiomegaly and enlarged cardiomeastinum’’ in the CheXpert dataset are diseases related to the heart. The rest of the pathologies in both datasets are associated with the

TABLE II: PATHOLOGY-WISE PERFORMANCE COMPARISON OF THE PROPOSED METHOD WITH STATE-OF-THE-ART SYSTEMS ON THE NIH DATASET. THE 14 FINDINGS FOR NIH DATASETS ARE EMPHYSEMA (EMPH), FIBROSIS (FIBR), HERNIA (HERN), INFILTRATION (INFI), PLEURAL THICKENING (PT), MASS, NODULE (NODU), ATELECTASIS (ATEL), CARDIOMEGALY (CARD), CONSOLIDATION (CONS), EDEMA (EDEM), EFFUSION (EFFU), PNEUMONIA (PNE1), AND PNEUMOTHORAX (PNE2).

Method	Emph	Fibr	Hern	Infi	PT	Mass	Nodu	Atel	Card	Cons	Edem	Effu	Pne1	Pne2	Average
DCNN [5]	0.8150	0.7690	0.7670	0.6090	0.7080	0.7060	0.6710	0.7160	0.8070	0.7080	0.8350	0.7840	0.6330	0.8060	0.7381
LSTM-Net [29]	0.8420	0.7570	0.8240	0.6750	0.7240	0.7270	0.7780	0.7330	0.8580	0.7170	0.8060	0.8060	0.6900	0.8050	0.7673
TieNet [32]	0.8650	0.7960	0.8760	0.6660	0.7350	0.7250	0.6850	0.7320	0.8440	0.7010	0.8290	0.7930	0.7200	0.8470	0.7724
AGCL [10]	0.9075	0.8179	0.8747	0.6892	0.7647	0.8136	0.7545	0.7557	0.8865	0.7283	0.8475	0.8191	0.7292	0.8499	0.8027
Ho <i>et al.</i> [33]	0.8750	0.7560	0.8360	0.7030	0.7740	0.8350	0.7160	0.7950	0.8870	0.7860	0.8920	0.8750	0.7420	0.8630	0.8097
SDFN [34]	0.9210	0.8350	0.9110	0.7000	0.7910	0.8150	0.7650	0.7810	0.8850	0.7430	0.8420	0.8320	0.7190	0.8660	0.8150
CRAL [12]	0.9080	0.8300	0.9170	0.7020	0.7780	0.8340	0.7730	0.7810	0.8800	0.7540	0.8500	0.8290	0.7290	0.8570	0.8159
CheXNet [15]	0.9249	0.8219	0.9323	0.6894	0.7925	0.8307	0.7814	0.7795	0.8816	0.7542	0.8496	0.8268	0.7354	0.8513	0.8180
DualCheXNet [35]	0.9420	0.8370	0.9120	0.7050	0.7960	0.8380	0.7960	0.7840	0.8880	0.7460	0.8520	0.8310	0.7270	0.8760	0.8230
LLAGNet [11]	0.9390	0.8320	0.9160	0.7030	0.7980	0.8410	0.7900	0.7830	0.8850	0.7540	0.8510	0.8340	0.7290	0.8770	0.8237
Wang <i>et al.</i> [13]	0.9330	0.8380	0.9380	0.7100	0.7910	0.8340	0.7770	0.7790	0.8950	0.7590	0.8550	0.8360	0.7370	0.8780	0.8260
Yan <i>et al.</i> [16]	0.9422	0.8326	0.9341	0.7095	0.8083	0.8470	0.8105	0.7924	0.8814	0.7598	0.8470	0.8415	0.7397	0.8759	0.8302
Luo <i>et al.</i> [36]	0.9396	0.8381	0.9371	0.7184	0.8036	0.8376	0.7985	0.7891	0.9069	0.7681	0.8610	0.8418	0.7419	0.9063	0.8349
Proposed Anatomy X-Net	0.9227	0.8322	0.9622	0.7051	0.7856	0.8553	0.7932	0.8150	0.9080	0.8096	0.8957	0.8803	0.7751	0.8741	0.8439

TABLE III: PATHOLOGY-WISE PERFORMANCE COMPARISON OF THE PROPOSED METHOD WITH STATE-OF-THE-ART SYSTEMS ON THE CHEXPART DATASET.

Method	Atelectasis	Cardiomegaly	Edema	Consolidation	Pleural Effusion	Average
DeneseNet-121 without any AAA and PWAP modules	0.75	0.80	0.89	0.83	0.88	0.820
CheXpert Official Benchmark [17]	0.81	0.84	0.93	0.93	0.93	0.889
Pham <i>et al.</i> [37]	0.81	0.83	0.93	0.93	0.92	0.884
Proposed Anatomy X-Net	0.87	0.86	0.93	0.88	0.92	0.902

lungs. To utilize this criterion, we apply BCE loss function on attention vectors by,

$$L_{attn} = -\frac{1}{nC} \sum_{j=1}^n \sum_{i=1}^C \left[(l_j)_i \log \{(v_j)_i\} + \{1 - (l_j)_i\} \log \{1 - (v_j)_i\} \right]. \quad (20)$$

Here, $n = 2$ representing A_{LE} and A_{HE} attention vectors respectively. $(v_j)_i$ and $(l_j)_i$ represent the sigmoid function activated value and ground truth label of the j^{th} attention vectors at position i , where $i \in \{1, 2, \dots, C\}$ and $j \in \{1, 2\}$. For lung related pathologies, ground truth vector l_i for A_{LE} attention vector is a vector of dimension C , where each of the value is 1. Otherwise, every values of l_i is 0. Similar case follows for heart related pathologies. Finally we find the total loss by,

$$L_{total} = L_{cls} + \lambda_{pa} L_{attn}. \quad (21)$$

Here, λ_{pa} is a hyper-parameter of our framework. We let $\lambda_{pa} = 0.2$, which is selected empirically.

Preprocessing and Hyper-parameters: We resize the original images to 256×256 and normalize them with the mean and standard deviation of the ImageNet training set. We randomly crop a 224×224 sub-image during training to augment the original training subset. For a fairer comparison, we follow [16] and take advantage of flipping and scaling to increase the variation and the diversity of training samples. For validation and inference, we use a centrally cropped sub-image of 224×224 dimensions as input. The anatomy masks from the segmentation network are resized to 84×84 before passing to the AAA modules. We use Adam optimizer [40] with standard parameters ($\beta_1 = 0.9$ and $\beta_2 = 0.99$). The batch size is set to

44 with a gradient accumulation step of 2. We set the initial learning rate 0.0001 and run the training for 14 epochs.

Performance Metric: Following previous studies, [5], [36], we employ the area under the receiver operating characteristic curve (AUC) for performance evaluation. The AUC of each disease class is evaluated as well as the average AUC overall categories. We validate the model in every epoch on the validation dataset and choose the model with the highest validation AUC for evaluation on the test dataset.

V. EXPERIMENTAL RESULTS AND ANALYSIS

A. Performance on NIH-dataset

We compare our proposed Anatomy X-Net with previously published state-of-the-art methods including: deep convolutional neural networks (DCNN) [5], deep network with long-short-term-memory unit (LSTM-Net) [29], TextImage Embedding network (TieNet) [32], Attention-Guided Curriculum Learning (AGCL) [10], the method presented by Ho *et al.* [33], Segmentation-Based Deep Fusion Network (SDFN) [34], Category-wise Residual Attention Learning (CRAL) [12], CheXNet [15], DualCheXNet [35], Lesion location Attention Guided Network (LLAGNet) [11], the method of Wan *et al.* [13], Yan *et al.* [16], and Luo *et al.* [36].

Our model achieves an average AUC score of 0.8401 without any augmentation during inference and exceeds all the compared models. For a fairer comparison, we follow [16], [36], and take advantage of horizontal flipping and cropping at five different positions to augment the test data and using average probabilities of ten cropped sub-images (four corner crops and one central crop plus horizontally flipper version of these) as the final prediction. As shown in Table II, the

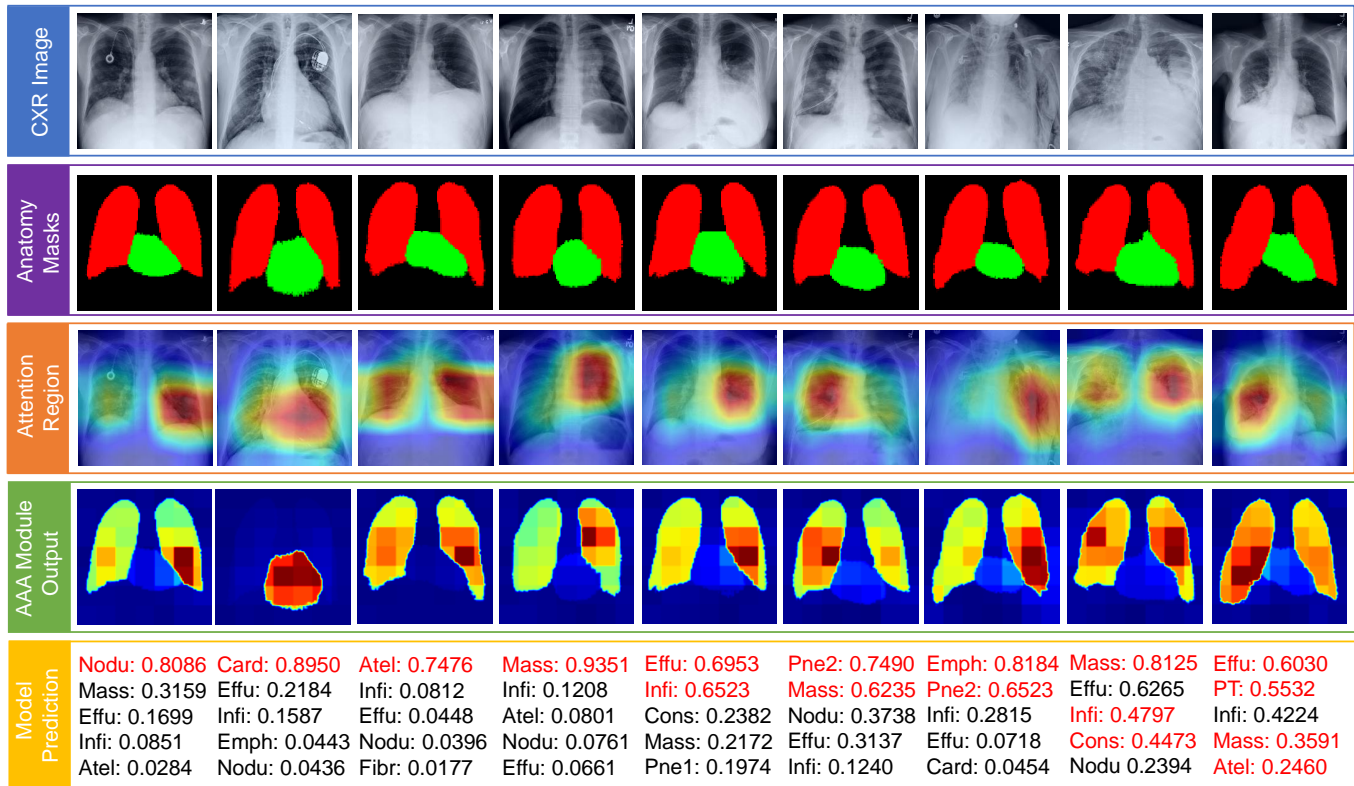


Fig. 4: The first row depicts the CXR images from the NIH test dataset. The Anatomy masks derived from the segmentation model in a semi-supervised way are shown in the second row. The third row depicts the attention regions derived from the feature map encoded by the dense block-4 of the backbone model. The fourth row demonstrates the output of the AAA module that works on the feature space from dense block-4. This AAA module integrates anatomy information into the Anatomy X-Net. The final row shows top-5 predicted findings and the corresponding prediction scores of Anatomy X-net. The ground truth labels are highlighted in red.

method proposed by Luo et al. [36] is the previous state-of-the-art yielding an AUC of 0.8349, while our method exceeds all the compared models and achieves a new state-of-the-art performance of 0.8439 AUC. Specifically, our classification results outperform others in 8 out of 14 categories. In the rest of the six categories, our model achieved slightly worse but competitive scores. Overall, the proposed Anatomy X-Net achieves a 1.0778% relative improvement in average AUC over the former best system by integrating the anatomy knowledge.

B. Performance on CheXpert-dataset

To demonstrate the generalizability of our method, we carry out experiments on the CheXpert official validation dataset as well. First, we report the baseline model performance, DenseNet-121, without any AAA and PWAP modules. The baseline model does not use the prior anatomy segmentation information from the semi-supervised segmentation model. Next, we report the performance of the proposed Anatomy X-Net. Finally, we compare our performance with the U-Zeros method from CheXpert benchmark [17] and Pham et al. [37]. The experimental results are shown in Table III. The results show that our model achieved an AUC of 0.902, surpassing the

CheXpert benchmark of U-Zeros [17], and method presented in [37].

C. Analysis of attention regions and attention vectors

We demonstrate the attention regions and output of our proposed AAA module in Fig. 4, along with the CXR images, anatomy masks, and classification results. We produce the attention heat maps to visualize the most indicative pathology areas on CXRs from the test dataset, interpreting the representational power of Anatomy X-Net. Heatmaps in the third row in Fig. 4 are constructed from the feature space encoded by the dense block-4 of the Anatomy X-Net. The heatmaps are computed by averaging along the channel dimension. Then, they are normalized and resized to the original CXR image dimension. The fourth row demonstrates the output of the AAA module that works on the feature space derived from the dense block-4. A visual evaluation of the output generated by the AAA module confirms that the anatomy-awareness of the module. Thus, similar to the process followed by a radiologist, the AAA module integrates the anatomy information responsible for a particular pathology within the

model. The final row of Fig. 4 shows top-5 predicted findings and the corresponding prediction scores of Anatomy X-net.

D. Effectiveness of AAA modules

AAA modules are the driving blocks of our method that help the model learn the salient anatomy information associated with a particular thoracic disease. Our experiments find that classification performance improves from the baseline when we cascade a AAA module with a dense block. Here, the baseline denotes the backbone model, DenseNet-121, without any integrated AAA modules. However, adding an AAA module with all the dense blocks does not enhance the performance. Because low-level spatial features from dense block-1 and dense block-2 might have outlier information which deteriorates the model performance by causing the model to give attention to noisy information. Again, applying AAA only on the highest level of features, in our case dense block-4, does not guarantee the best performance. Because due to subsequent pooling in these dense blocks, some important information may be lost in the later dense blocks presented in the previous blocks. To evaluate the efficacy of this effect, we have tested different levels of anatomy-aware attention on the NIH dataset. First, we only used an AAA module with dense block-4. This experiment is denoted by anatomy aware attention level-1. After that, we used one AAA module with dense block-4 and another one with dense block-3. We denote this experiment by anatomy aware attention level-2. Finally, we applied the AAA module with dense blocks-2,3,4 and referred to it as anatomy aware attention level-3. The experimental results are provided in Table IV. The results show that classification performance improves when going from AAA level-1 to level-2 while it decreases when using level-3.

E. Effectiveness of PWAP modules

As discussed in Sec III-C, we have proposed a novel PWAP module with learnable parameters to tweak the relevant area of the feature space before pooling. To show the effectiveness of PWAP modules, we replace all the PWAP in Anatomy X-Net with average pooling, max pooling, and generalized mean pooling [41] respectively and run the experiment while keeping all the other hyperparameters the same. The results shown in Table V depicts the effectiveness of the proposed module. In Fig. 5, the feature space before and after passing through the PWAP layer is shown. The PWAP module tweaks the feature space to focus on the lesion areas more prominently by removing unwanted attention.

TABLE IV: COMPARISON OF THE EFFECTIVENESS OF INTEGRATING THE PROPOSED ANATOMY-AWARE ATTENTION (AAA) MODULE AT VARIOUS STAGES OF THE BACKBONE NETWORK.

Model	Block Configuration	AUC
AAA level-1	DenseBlock-4 + AAA Block	0.8348
AAA level-2	DenseBlock-3,4 + AAA Blocks	0.8401
AAA level-3	DenseBlock-2,3,4 + AAA Blocks	0.8371

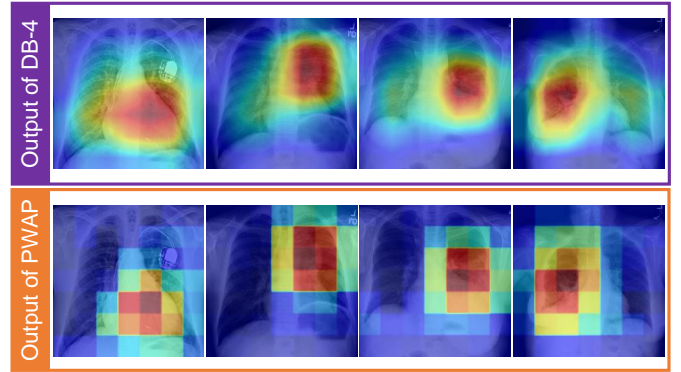


Fig. 5: Demonstration of feature space recalibration performed by the PWAP module. The first row depicts the feature space derived from the DB-4 block. The second row shows the recalibrated feature space by the PWAP module before pooling. The PWAP module tweaks the feature space to focus on the lesion areas more firmly by removing unwanted attention.

TABLE V: PERFORMANCE COMPARISON OF THE PROPOSED PROBABILISTIC WEIGHTED AVERAGE POOLING (PWAP) WITH OTHER POOLING METHODS ON THE NIH DATASET.

Pooling Type	AUC
Average Pooling	0.8388
Max Pooling	0.8341
Generalized Mean Pooling	0.8392
PWAP	0.8401

F. Effect of Anatomy Mask Dimension

Incorporating anatomy masks at their original resolution in high-level feature space maps encoded by dense blocks is computationally highly intensive. Due to hardware constraints, the feature spaces are up-sampled while masks are downsampled to an intermediate shape. We present the performance results of our proposed anatomy x-net on the different intermediate dimensions of anatomy masks in Table VI. Here, we observe that the performance of our model improves as we increase the dimension of the anatomy masks. This implies that, with the larger intermediate dimensions of anatomy masks, we can possibly further improve the performance of our proposed model.

TABLE VI: EFFECT OF ANATOMY MASK DIMENSION.

Mask Dimension	42×42	56×56	70×70	84×84
AUC	0.8353	0.8384	0.8388	0.8401

VI. CONCLUSION

In this paper, we propose a semi-supervised anatomy-aware convolutional neural network for thoracic disease classification named the Anatomy X-Net. Departing from the previous works that rely on the chest x-ray image only or attention mechanisms guided by the model prediction, the proposed network is guided by prior anatomy segmentation information to act similar to a radiologist by focusing on relevant anatomical regions associated with the thoracic disease. Extensive

experiments demonstrate that combining our novel AAA and PWAP modules within a backbone Densenet-121 model in a unified framework yields state-of-the-art performance on the NIH chest x-ray dataset. The Anatomy X-Net achieves an average AUC score of 0.8439 on the official NIH test set, surpassing the former best performing method published on this dataset. The proposed method also reaches an AUC of 0.9020 on the official validation split of the Stanford CheXpert dataset, providing improved performance compared to existing methods.

REFERENCES

- [1] S. Raouf, D. Feigin, A. Sung, S. Raouf, L. Irugupati, and E. C. Rosenow III, "Interpretation of plain chest roentgenogram," *Chest*, vol. 141, no. 2, pp. 545–558, 2012.
- [2] P. Yu, H. Xu, Y. Zhu, C. Yang, X. Sun, and J. Zhao, "An automatic computer-aided detection scheme for pneumoconiosis on digital chest radiographs," *J. Digit. Imaging*, vol. 24, no. 3, pp. 382–393, 2011.
- [3] S. Jaeger, A. Karargyris, S. Candemir, L. Folio, J. Siegelman, F. Callaghan, Z. Xue, K. Palaniappan, R. K. Singh, S. Antani *et al.*, "Automatic tuberculosis screening using chest radiographs," *IEEE Trans. Med. Imag.*, vol. 33, no. 2, pp. 233–245, 2013.
- [4] G. Litjens, T. Kooi, B. E. Bejnordi, A. A. A. Setio, F. Ciompi, M. Ghafoorian, J. A. Van Der Laak, B. Van Ginneken, and C. I. Sánchez, "A survey on deep learning in medical image analysis," *Med. Image Anal.*, vol. 42, pp. 60–88, 2017.
- [5] X. Wang, Y. Peng, L. Lu, Z. Lu, M. Bagheri, and R. M. Summers, "Chestx-ray8: Hospital-scale chest x-ray database and benchmarks on weakly-supervised classification and localization of common thorax diseases," in *Proc. IEEE CVPR*, 2017, pp. 3462–3471.
- [6] J. Deng, W. Dong, R. Socher, L. Li, Kai Li, and Li Fei-Fei, "Imagenet: A large-scale hierarchical image database," in *IEEE CVPR*, 2009, pp. 248–255.
- [7] S. Liu and W. Deng, "Very deep convolutional neural network based image classification using small training sample size," in *ACPR*, 2015, pp. 730–734.
- [8] C. Szegedy, Wei Liu, Yangqing Jia, P. Sermanet, S. Reed, D. Anguelov, D. Erhan, V. Vanhoucke, and A. Rabinovich, "Going deeper with convolutions," in *IEEE CVPR*, 2015, pp. 1–9.
- [9] K. He, X. Zhang, S. Ren, and J. Sun, "Deep residual learning for image recognition," in *IEEE CVPR*, 2016, pp. 770–778.
- [10] Y. Tang, X. Wang, A. P. Harrison, L. Lu, J. Xiao, and R. Summers, "Attention-guided curriculum learning for weakly supervised classification and localization of thoracic diseases on chest radiographs," in *MLMI@MICCAI*, 2018.
- [11] B. Chen, J. Li, G. Lu, and D. Zhang, "Lesion location attention guided network for multi-label thoracic disease classification in chest x-rays," *IEEE J. of Biomed. and Health Inform.*, pp. 2016–2027, 2020.
- [12] Q. Guan and Y. Huang, "Multi-label chest x-ray image classification via category-wise residual attention learning," *Pattern Recognit. Letters*, vol. 130, pp. 259–266, 2020.
- [13] H. Wang, S. Wang, Z. Qin, Y. Zhang, R. Li, and Y. Xia, "Triple attention learning for classification of 14 thoracic diseases using chest radiography," *Med. Image Anal.*, vol. 67, p. 101846, 2020.
- [14] C. Clarke and A. Dux, *Chest X-rays for medical students*. John Wiley & Sons, 2017.
- [15] P. Rajpurkar, J. Irvin, K. Zhu, B. Yang, H. Mehta, T. Duan, D. Ding, A. Bagul, C. Langlotz, K. Shpanskaya, M. Lungren, and A. Ng, "Chexnet: Radiologist-level pneumonia detection on chest x-rays with deep learning," *ArXiv*, vol. abs/1711.05225, 2017.
- [16] C. Yan, J. Yao, R. Li, Z. Xu, and J. Huang, "Weakly supervised deep learning for thoracic disease classification and localization on chest x-rays," in *Proc. ACM Int. Conf. on Bioinformatics, Computational Biology, and Health Informatics*, 2018.
- [17] J. Irvin, P. Rajpurkar, M. Ko, Y. Yu, S. Ciurea-Ilcus, C. Chute, H. Marklund, B. Haghighi, R. Ball, K. Shpanskaya *et al.*, "Chexpert: A large chest radiograph dataset with uncertainty labels and expert comparison," in *Proc. AAAI Artif. Intell.*, 2019, pp. 590–597.
- [18] A. Mondal, A. Agarwal, J. Dolz, and C. Desrosiers, "Revisiting cyclegan for semi-supervised segmentation," *ArXiv*, vol. abs/1908.11569, 2019.
- [19] J. Shiraishi, S. Katsuragawa, J. Ikezoe, T. Matsumoto, T. Kobayashi, K. Komatsu, M. Matsui, H. Fujita, Y. Kodera, and K. Doi, "Development of a digital image database for chest radiographs with and without a lung nodule: receiver operating characteristic analysis of radiologists' detection of pulmonary nodules," *AJR Am. J. Roentgenol.*, vol. 174 1, pp. 71–4, 2000.
- [20] Y. Shao, Y. Gao, Y. Guo, Y. Shi, X. Yang, and D. Shen, "Hierarchical lung field segmentation with joint shape and appearance sparse learning," *IEEE Trans. Med. Imag.*, vol. 33, no. 9, pp. 1761–1780, 2014.
- [21] B. van Ginneken, M. B. Stegmann, and M. Loog, "Segmentation of anatomical structures in chest radiographs using supervised methods: a comparative study on a public database," *Med. Image Anal.*, vol. 10, no. 1, pp. 19–40, 2006.
- [22] B. Ibragimov, B. Likar, F. Pernuš, and T. Vrtovec, "Accurate landmark-based segmentation by incorporating landmark misdetections," in *IEEE ISBI*, 2016, pp. 1072–1075.
- [23] T. Xu, M. Mandal, R. Long, I. Cheng, and A. Basu, "An edge-region force guided active shape approach for automatic lung field detection in chest radiographs," *Comput. Med. Imaging Graph.*, vol. 36, no. 6, pp. 452–463, 2012.
- [24] M. Kholiavchenko, I. Sirazitdinov, K. Kubrak, R. Badrutdinova, R. Kuleev, Y. Yuan, T. Vrtovec, and B. Ibragimov, "Contour-aware multi-label chest x-ray organ segmentation," *Int. J. Comput. Assist. Radiol. Surg.*, vol. 15, no. 3, pp. 425–436, 2020.
- [25] F. Munawar, S. Azmat, T. Iqbal, C. Gr' onlund, and H. Ali, "Segmentation of Lungs in Chest X-Ray Image Using Generative Adversarial Networks," *IEEE Access*, vol. 8, pp. 153 535–153 545, 2020.
- [26] J. C. Souza, J. O. B. Diniz, J. L. Ferreira, G. L. F. da Silva, A. C. Silva, and A. C. de Paiva, "An automatic method for lung segmentation and reconstruction in chest x-ray using deep neural networks," *Comput. Methods Programs Biomed.*, vol. 177, pp. 285–296, 2019.
- [27] A. Tolkaev, I. Sirazitdinov, M. Kholiavchenko, T. Mustafaev, and B. Ibragimov, "Deep Learning for Diagnosis and Segmentation of Pneumothorax: The Results on The Kaggle Competition and Validation Against Radiologists," *IEEE J. Biomed. Health Inform.*, 2020.
- [28] H.-J. Chen, S.-J. Ruan, S.-W. Huang, and Y.-T. Peng, "Lung X-ray Segmentation using Deep Convolutional Neural Networks on Contrast-Enhanced Binarized Images," *Mathematics*, vol. 8, no. 4, p. 545, 2020.
- [29] L. Yao, E. Poblens, D. Dagunts, B. Covington, D. Bernard, and K. Lyman, "Learning to diagnose from scratch by exploiting dependencies among labels," *ArXiv*, vol. abs/1710.10501, 2017.
- [30] G. Huang, Z. Liu, L. Van Der Maaten, and K. Q. Weinberger, "Densely connected convolutional networks," in *IEEE CVPR*, 2017, pp. 2261–2269.
- [31] H. Sak, A. W. Senior, and F. Beaufays, "Long short-term memory recurrent neural network architectures for large scale acoustic modeling," in *INTERSPEECH*, 2014, pp. 338–342.
- [32] X. Wang, Y. Peng, L. Lu, Z. Lu, and R. Summers, "Tienet: Text-image embedding network for common thorax disease classification and reporting in chest x-rays," *IEEE CVPR*, pp. 9049–9058, 2018.
- [33] T. K. K. Ho and J. Gwak, "Multiple feature integration for classification of thoracic disease in chest radiography," *Appl. Sci.*, vol. 9, no. 19, p. 4130, 2019.
- [34] H. Liu, L. Wang, Y. Nan, F. Jin, Q. Wang, and J. Pu, "SDFN: Segmentation-based deep fusion network for thoracic disease classification in chest x-ray images," *Comput. Med. Imaging Graph.*, vol. 75, pp. 66–73, 2019.
- [35] B. Chen, J. Li, X. Guo, and G. Lu, "DualCheXNet: dual asymmetric feature learning for thoracic disease classification in chest x-rays," *Biomed. Signal Process. and Control*, vol. 53, p. 101554, 2019.
- [36] L. Luo, L. Yu, H. Chen, Q. Liu, X. Wang, J. qi Xu, and P. Heng, "Deep mining external imperfect data for chest x-ray disease screening," *IEEE Trans. Med. Imag.*, pp. 3583–3594, 2020.
- [37] H. H. Pham, T. T. Le, D. Q. Tran, D. T. Ngo, and H. Q. Nguyen, "Interpreting chest x-rays via cnns that exploit hierarchical disease dependencies and uncertainty labels," *Neurocomputing*, 2021.
- [38] S. Ioffe and C. Szegedy, "Batch normalization: Accelerating deep network training by reducing internal covariate shift," in *Proc. ICML*, 2015, pp. 448–456.
- [39] J. Hu, L. Shen, and G. Sun, "Squeeze-and-excitation networks," in *IEEE CVPR*, 2018, pp. 7132–7141.
- [40] D. P. Kingma and J. Ba, "Adam: A method for stochastic optimization," *CoRR*, vol. abs/1412.6980, 2015.
- [41] M. Berman, H. Jégou, A. Vedaldi, I. Kokkinos, and M. Douze, "Multi-grain: a unified image embedding for classes and instances," *ArXiv*, vol. abs/1902.05509, 2019.